Pergamon

Acta mater. Vol. 46, No. 10, pp. 3501–3510, 1998

Printed in Great Britain
PII: S1359-6454(98)00035-4
1359-6454/98 $19.00 + 0.00

MATHEMATICAL MODELLING OF THE MECHANICAL ALLOYING KINETICS

S. K. PABI, D. DAS, T. K. MAHAPATRA and I. MANNA

Department of Metallurgical and Materials Engineering, Indian Institute of Technology, Kharagpur 721302, India

(Received 20 January 1997; accepted 10 January 1998)

Abstract—A rigorous mathematical model, based on the modified *iso*-concentration contour migration method, has been developed to predict the kinetics of diffusive intermixing in a binary miscible system in the course of mechanical alloying (MA). The present model considers the variation of diffusion coefficient with composition, and interface shift due to both interdiffusion and mechanical deformation. Comparison of the kinetics predicted by the present model with the relevant experimental data from Cu–Ni and Cu–Zn shows that the effective mass transport operative in MA attains a rate intermediate between that for volume or grain boundary diffusion. An effective temperature for diffusion (T_{eff}) has been proposed to simulate the observed alloying kinetics. T_{eff} is a function of composition but is not related to the adiabatic temperature rise at the point of ball-powder collision. Finally, the ratio of T_{eff} to the corresponding liquidus temperature for all the composition studied lies between 0.4 and 0.5. © *1998 Acta Metallurgica Inc.*

1. INTRODUCTION

Nanostructured materials have received wide attention in the recent times as they may possess metastable microstructure with novel ranges of property [1–3]. Mechanical alloying (MA) by high energy ball milling is an easy and inexpensive route of producing nanostructured materials in bulk quantities with excellent scope of microstructural and process control [4–10]. In MA of ductile metals, the powder particles trapped between the colliding balls and vial undergo simultaneous deformation, fragmentation, and cold welding [8, 11] resulting into agglomerates of multilayered structures with clean interfaces [11–15]. Intermixing in such an aggregate during high energy ball milling often leads to the extension of solid solubility limit, and formation of nanostructured alloys, intermetallic compounds and amorphous phases [8, 16–18].

In the past, several attempts have been made to model the process/mechanism of MA [8, 18–22]. But only a few studies have been reported on mathematical modelling of the kinetics of MA [23–26]. During high energy ball milling, alloying may take place through (at least) two different mechanisms, namely, gradual diffusive intermixing and discontinuous additive mixing [27, 28]. The present model concerns the kinetics of alloying through the former mechanism only. Schultz *et al.* [23] have developed a simple kinetic model for solid state amorphization in Ni–Zr by MA. It has been assumed that Ni disperses rapidly along the boundaries of Zr grains of experimentally determined minimum size, and subsequently, undergoes bulk diffusion towards the center of the Zr particles leading to solid state amorphization. The kinetic analysis is therefore reduced to solving the diffusion equation for a Zr particle surrounded by a semi-infinite medium of Ni. Dupeux *et al.* [24] have considered the chemical interdiffusion characteristics within the multilayered structure generated during MA as equivalent to that in sandwich specimens of alternate polycrystalline slices of Ni bonded to stoichiometric Ni_3Al. Similar simplistic solution for homogenization in MA has also been presented by Courtney *et al.* [25]. However, all these models [23–25] make several simplifying assumptions in solving the mass balance equation and fail to consider the change in the diffusion field width caused by deformation during MA.

Martin and coworkers [21, 29, 30] have suggested that phase transformation in an externally driven system such as high energy ball milling needs to be analyzed from the point of view of a nonequilibrium dynamical situation. Bellon and Averback [31] have proposed that mass transport during MA may take place by two simultaneously operating mechanisms, namely, atomic transport due to shear along randomly selected glide planes as well as thermally activated diffusion of the constituent atoms. If the former process is dominant, the atomic mobility term in this approach may not be related to the melting/liquidus temperature of the system. Such a model may provide an explanation for alloying induced by ball milling in the immiscible systems.

During MA in ductile and miscible (completely/partially) systems, deformation leads to a change in the thickness of the constituent phases, that in turn distorts the concentration profiles. Moreover, the

interface also shifts due to concurrent intermixing of the constituent atoms diffusing at different rates. As a result, the MA kinetics transforms into a special moving boundary problem. In this paper, a rigorous numerical solution of this problem has been presented. The present model simultaneously takes into account the variation of the interdiffusion coefficient (D) with composition (C), and interface shift due to both diffusion as well as deformation. The results predicted by the model have been compared with the relevant experimental data from the Cu–Ni and Cu–Zn systems to yield a measure of the enhanced/effective mass transfer rate operating during MA.

2. THE MODEL

The present model on MA kinetics is based on a modified version of the *iso*-concentration contour migration (ICCM) method [32], developed earlier to estimate the rate of diffusion controlled dissolution in a two-phase planar and multilayered aggregate. This modified ICCM (henceforth to be referred as the MICCM) method is capable of considering the deformation induced changes in diffusion distances while calculating the alloying kinetics. Here the extent or rate of deformation of the constituent phases need not be identical. For this purpose, the diffusion equations have been suitably transformed to express the distance (X) as a function of concentration (C) and time (t), such that C is an independent variable. As the solute concentration at the interface remains constant in a diffusion controlled alloying process, this transformation converts the moving boundary problem into a static boundary one, even in the presence of mechanical deformation accompanying the MA process. Here, X is computed at any t in two discrete steps, at first to consider diffusive intermixing, and subsequently, to incorporate the constraints of concurrent deformation accompanying MA.

2.1. Calculation of the diffusional mass transfer

Formation of a layered structure during MA of ductile ingredients has been reported by several investigators [11–15]. Figure 1 schematically shows the cross-section of such a layered structure composed of uniformly sized and homogeneous plates of A and B phases. The broken lines represent the location of the symmetry planes signifying no net mass transfer across them. In view of the symmetrical and repetitive configuration, a sandwich structure consisting of two adjacent halves of the A and B layers may constitute a representative element for numerical analysis. The concentration profile in such an element of initial half width, W ($=W_A+W_B$) at $t=0$ in the course of MA is schematically illustrated in Fig. 2. The volume fraction of A at the beginning of MA (i.e. $t=0$) is W_A/W (Fig. 2(a)). Figures 2(b) and (c) schematically illus-

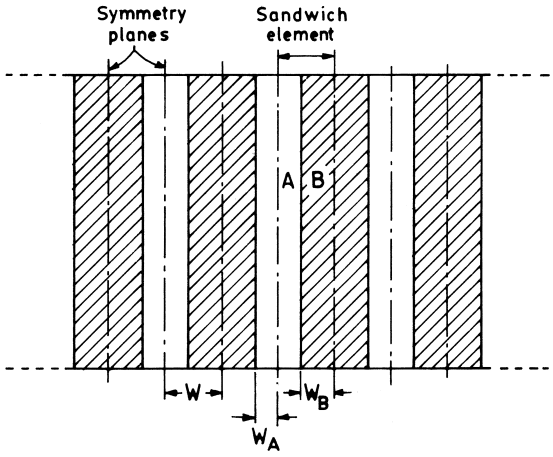

Fig. 1. Schematic view of the cross-section of a layered structure of a ductile ball-milled aggregate.

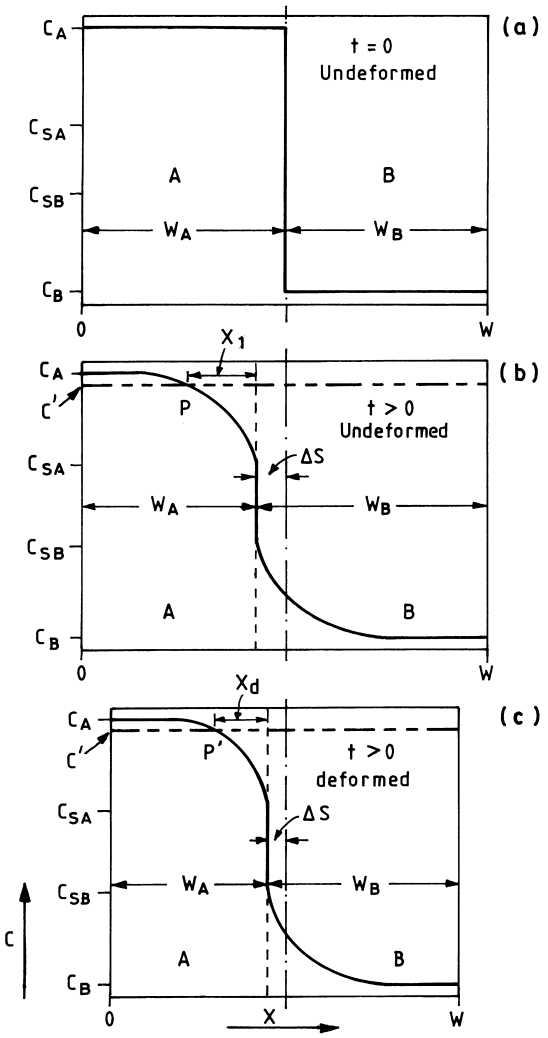

Fig. 2. Evolution of concentration–distance profile across a sandwich element: (a) prior to interdiffusion, (b) following interdiffusion without incorporating deformation of the phases, and (c) after considering both interdiffusion and dimensional changes due to mechanical deformation in MA.

trate how the respective interdiffusion and superimposed deformation affect the distance–concentration profile and interface shift with respect to the original position of the interface. Since W_A or W_B is much smaller than their respective lengths, the scheme of mixing may be considered as a one-dimensional diffusion problem having the field equation:

$$\frac{\partial C}{\partial t} = \frac{\partial}{\partial X}\left(D\frac{\partial C}{\partial X}\right) \tag{1}$$

where, C is the dependent variable and D the diffusion coefficient. Since the concentration along an *iso*-concentration contour is constant,

$$dC = \left(\frac{\partial C}{\partial X}\right)dX + \left(\frac{\partial C}{\partial t}\right)dt = 0 \tag{2}$$

and therefore,

$$\left(\frac{\partial C}{\partial t}\right) = -\left(\frac{\partial C}{\partial X}\right)\left(\frac{\partial X}{\partial t}\right). \tag{3}$$

It may be readily shown that,

$$\frac{\partial}{\partial X}\left(D\frac{\partial C}{\partial X}\right) = \left(\frac{\partial D}{\partial C}\right)\left(\frac{\partial X}{\partial C}\right)^{-2} - D\left(\frac{\partial^2 X}{\partial C^2}\right)\left(\frac{\partial X}{\partial C}\right)^{-3}. \tag{4}$$

Substitution of equations (3) and (4) to the field equation (1) with proper subscripts and superscripts yields the following set of coupled partial differential equations for the A-phase:

$$\frac{\partial X}{\partial t} = D^A\left(\frac{\partial^2 X}{\partial C_A^2}\right)\left(\frac{\partial X}{\partial C_A}\right)^{-2} - \left(\frac{\partial D^A}{\partial C_A}\right)\left(\frac{\partial X}{\partial C_A}\right)^{-1} \tag{5}$$

and for the B-phase:

$$\frac{\partial X}{\partial t} = D^B\left(\frac{\partial^2 X}{\partial C_B^2}\right)\left(\frac{\partial X}{\partial C_B}\right)^{-2} - \left(\frac{\partial D^B}{\partial C_B}\right)\left(\frac{\partial X}{\partial C_B}\right)^{-1} \tag{6}$$

where, D^A and D^B are the interdiffusion coefficients, and C_A and C_B the compositions of A and B, respectively. Since the dimension of the sandwich element may change due to deformation, the interface between A and B phases representing the concentration invariant location is taken as the reference ($X = 0$) in the computation. Therefore, the boundary conditions for finite geometry of the sandwich element are:

$$\frac{\partial X}{\partial C_A} \longrightarrow \infty, \quad \text{at } X \longrightarrow -W_A,\ t \geq 0 \tag{7}$$

$$\frac{\partial X}{\partial C_B} \longrightarrow \infty, \quad \text{at } X \longrightarrow W_B,\ t \geq 0 \tag{8}$$

It may be pointed out that W_A and W_B do not remain constant in the course of MA. But W_A/W_B would not be affected, if the shear strain in both the phases are identical. The present model, however, allows the strain to be inequal in the two constituent phases. The condition of diffusional mass balance across the interface can be written as:

$$\frac{\partial S}{\partial t} = \frac{1}{C_{SA} - C_{SB}}\left[D^B\left(\frac{\partial C_B}{\partial X}\right)_{X=0} - D^A\left(\frac{\partial C_A}{\partial X}\right)_{X=0}\right] \tag{9}$$

where, C_{SA} and C_{SB} are the respective compositions of the A and B phases at the interface.

Computations have been carried out on a distance–concentration grid as shown in Fig. 3, which also illustrates the grid nomenclature. Here the respective composition ranges of the A and B phases have been divided into u and r equally spaced intervals, where $u = (g - e)$. According to the finite difference method of calculation, the respective derivatives of equations (5), (6) and (9) at a given time t_1 may be expressed as:

$$\frac{X1_i^{n+1} - X1_i^n}{\Delta t} = 4D_i^A\left[\frac{X1_{i+1}^n - 2X1_i^n + X1_{i-1}^n}{(X1_{i+1}^n - X1_{i-1}^n)^2}\right] - \left[\frac{D_{i+1}^A - D_{i-1}^A}{X1_{i+1}^n - X1_{i-1}^n}\right], \quad i = e,\ e+1,\ \ldots,\ f,\ g-1 \tag{10}$$

$$\frac{X1_i^{n+1} - X1_i^n}{\Delta t} = 4D_i^B\left[\frac{X1_{i+1}^n - 2X1_i^n + X1_{i-1}^n}{(X1_{i+1}^n - X1_{i-1}^n)^2}\right] - \left[\frac{D_{i+1}^B - D_{i-1}^B}{X1_{i+1}^n - X1_{i-1}^n}\right], \quad i = 1,\ 2,\ \ldots,\ q,\ r \tag{11}$$

where $X1_i^n$ is the distance of the contour G_i from the A/B-interface (cf. Fig. 3) at an instant $t_1 = n\Delta t$, n being an integer and Δt the time increment of t. If ΔS is extent of increment in W_B at $t_2 = (n + 1)\Delta t$ due to diffusion alone, then

$$\frac{\Delta S}{\Delta t} = \frac{2}{(C_{SA} - C_{SB})} \times \left[\frac{D_1^B \Delta C_B}{X1_3^n - 4X1_2^n + 3X1_1^n} - \frac{D_e^A \Delta C_A}{-X1_{e+2}^n + 4X1_{e+1}^n - 3X1_e^n}\right]. \tag{12}$$

It is evident from equations (10)–(12) that a unique value of D (say, D_i) may be assigned to each concentration grid point (G_i) during computation that automatically takes care of the variation of D with C. The stability conditions of the algorithm and method of initiation of calculation in the present model are analogous to that in the ICCM model [32]. In the present finite difference formulation, the boundary conditions (equations (7) and (8)) can be incorporated by fitting a parabola to the last three grid points. Thus, for the A-phase:

$$X1_g^{n+1} = (\sqrt{2}X1_{g-1}^{n+1} - X1_{g-2}^{n+1})/(\sqrt{2} - 1) \tag{13}$$

and for the B-phase,

$$X1_{r+1}^{n+1} = (\sqrt{2}X1_r^{n+1} - X1_{r-1}^{n+1})/(\sqrt{2} - 1). \tag{14}$$

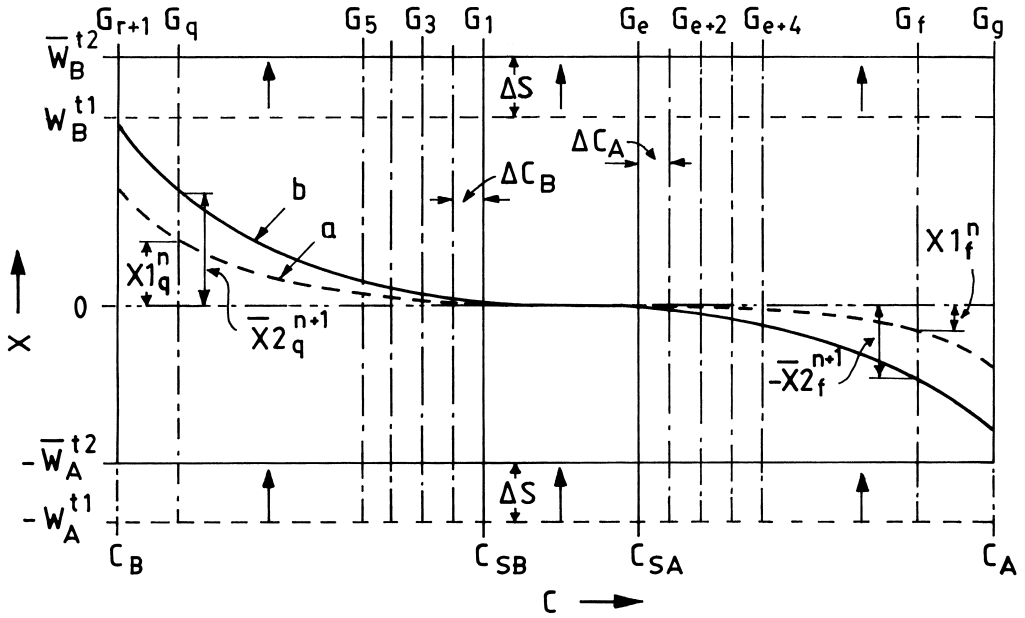

Fig. 3. Illustration of the finite difference terminology used in the MICCM model. Curve-a and curve-b represent the schematic plots of distance (X)-concentration (C) profile at time t_1 and following interdiffusion at t_2, respectively.

As none of the contours of the B-phase can physically go beyond W_B, (i.e. $X1_{r+1}^n \leq W_B^{t_1}$), a grid point G_{r+1} is discarded, as soon as the $X1_{r+1}^n$, exceeds $W_B^{t_1}$. In this situation, the value of X at the last grid point $X1_r^{n+1}$ is computed by fitting a parabola to $X1_r^n$, $X1_{r-1}^n$ and $X1_{r-2}^n$. Thus,

$$X1_r^{n+1} = X1_r^n + D^B \Delta t/(W_B^{t_1} - X1_r^n). \qquad (15)$$

Similarly the grid point G_g is ignored when $X1_g^{n+1} > W_A^{t_1}$ in A, and consequently,

$$X1_{g-1}^{n+1} = X1_{g-1}^n - D^A \Delta t/X1_{g-1}^n. \qquad (16)$$

In Fig. 3, curve-a schematically shows the distance–concentration profile at a given time t_1 and curve-b after interdiffusion and consequent change in W_A and W_B at time t_2. Here $W_A^{t_1}$ and $W_B^{t_1}$ are the half-widths of A and B phases at t_1, respectively. The new half widths at t_2 is defined as: $\bar{W}_A^{t_2}(=W_A^{t_1}+\Delta S)$ and $\bar{W}_B^{t_2}(=W_B^{t_1}-\Delta S)$ for A and B, respectively. Since $X = 0$ at the A/B interface, the distance of the contour G_i after interdiffusion is redefined as $\bar{X}2_i^{n+1}$, such that $\bar{X}2_i^{n+1}(=X1_i^{n+1}-\Delta S)$ and $\bar{X}2_i^{n+1}(=X1_i^{n+1}+\Delta S)$ for the A and B phase, respectively.

2.2. *Superimposed effect of deformation on intermixing*

Figure 2(c) schematically shows the reduction in the widths of A and B phases following the impact of the colliding balls on the layered structure and consequent modification in the concerned concentration profiles. Plastic deformation is expected to expedite intermixing of the constituents atoms at the interface between the adjacent layers and thereby, reduce the composition difference across the interface ($\Delta C = C_{SA} - C_{SB}$). The ΔC is a function of the transient/metastable solubility limits of the phases concerned. In this regard, it may be noted that a considerable extension of solid solubility limit by extensive deformation in ball milling has been observed in Ni–Al [33, 34], but not in Cu–Zn [35]. On the other hand, atomic transport from the interface to the interior of a layer has to take place by diffusion, which may be enhanced by deformation induced "mechanical interdiffusion", as proposed by Rouff and Balluffi [36]. The mechanical deformation changes the relative position of the *iso*-concentration profiles. For instance, the point P having any particular concentration C' located at distance x_1 from the interface (Fig. 2(b)) would be shifted by uniform shear to a position P′, located at a distance x_d ($< x_1$) from the same interface (Fig. 2(c)). As a consequence, the concentration–distance profile within a layer appears steeper due to deformation at that instant (cf. Fig. 2(c) *vis-à-vis* Fig. 2(b)). It may be pointed out that the change in composition profile during a given interval of time is essentially the resultant the contributions rising out of diffusion (Fig. 2(b)) and deformation (Fig. 2(c)). While deformation tends to make the profile steeper, concurrent diffusion would tend to flatten the same. In any case, the concentration–distance profile becomes shallower with the progress of MA. For instance, curve-a (shown by broken line in Fig. 4) schematically represents the resultant composition profile at time t'. At a later instant of time t'' ($> t'$), the same profile becomes shallower

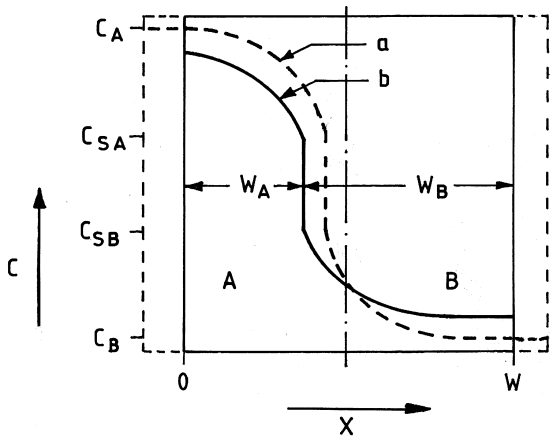

Fig. 4. Effect of time on *iso*-concentration contour representing the combined contributions of diffusion and deformation. Note that curve-a and curve-b correspond to time t' and t'' ($> t'$), respectively.

(curve-b in Fig. 4) due to the combined effect of diffusion and deformation accompanying the MA process.

In a distance–concentration plot (Fig. 3), the position of a given *iso*-concentration line after deformation in the interval (t_2–t_1) during MA may easily be determined by multiplying $\bar{X}2_i^{n+1}$ by a scaling factor. For phase A, the scaling factor for the time interval (t_2–t_1) is defined as: $\eta_A = W_A^{t_2}/W_A^{t_1}$, where $W_A^{t_1}$ and $W_A^{t_2}$ are the widths of the A-layer before and after deformation, respectively. The η_B for phase-B can be defined in a similar manner. Figure 5 shows the *iso*-concentration contour at t_2 before (curve-a) and after (curve-b) deformation. Accordingly, the new position of the contour at any grid point G_i in A and B-phase after deformation are $X2_i^{n+1} = \bar{X}2_i^{n+1}\,\eta_A$, and $X2_i^{n+1} = \bar{X}2_i^{n+1}\,\eta_B$, respectively. It may be pointed out that $\partial X/\partial C \to \infty$ at the symmetry planes, and therefore, remains unchanged by the multiplication with η_A or η_B. Hence, the boundary conditions (equations (7) and (8)) imposed by the finite geometry remain unaffected by the deformation process.

In numerical computation, the simultaneous deformation and interdiffusion are taken into account by incorporating a finite extent of dimensional change after solving the equations (10)–(14) at every Δt interval. After computation of $X2$ values at the $(n+1)$th time step, these are taken as the new value of $X1$ before solving the equations (10)–(14) for the next time step. When the number of workable grid points in any phase drops to less than three, the concentration profile in it is taken to be linear for introducing one new grid point at the midpoint between two nodes. The computation is terminated either when the width of a given phase measures less than 10^{-3} times its initial width, or composition gradient disappears in both the phases. Finally, the average composition of each phase at a given t has been computed by dividing the area under the X vs C plot by the corresponding instantaneous phase width.

3. EXPERIMENTAL

Two Cu–Ni alloys of nominal compositions $Cu_{50}Ni_{50}$, and $Cu_{20}Ni_{80}$ were produced by ball milling pure (> 99.5 wt%) elemental powders of Cu and Ni of -325 mesh size in a Fritsch Pulverisette

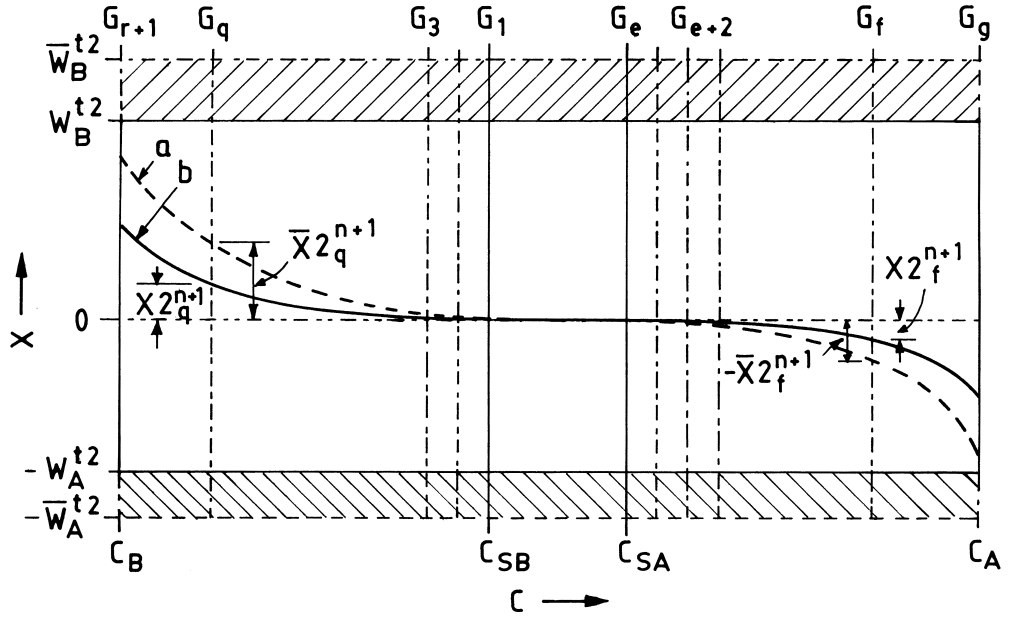

Fig. 5. Schematic distance (X)-concentration (C) profiles at t_2. Curve-a and curve-b represent the profiles after considering interdiffusion alone, and its modification by incorporating deformation, respectively.

5/2 high energy planetary ball mill. Milling was carried out at a mill speed (Ω) of 300 rpm in toluene medium using hardened chrome steel (Fe-12 wt% Cr-2 wt% C) container and balls of 10 mm diameter with a ball to powder ratio of 10:1.

The milled powders were characterized at various stages of milling by X-ray diffraction (XRD) analysis obtained from a Phillips PW 1710 diffractometer with Co–K_α radiation. The crystallite size (i.e. coherence length) was determined from the XRD line profile analysis of the (220) reflection by variance method [37, 38]. The extent of Ni dissolved in Cu (say, Cu_{Ni}) and vice versa (Ni_{Cu}) were determined by the peak shift analysis of the Cu and Ni peaks with respect to the standard data for the same reported in the literature [39]. The morphology and microstructure of the milled product were examined with a CAM SCAN2 scanning electron microscope (SEM).

4. RESULTS AND DISCUSSION

4.1. Crystallite size

Figure 6 shows the variation of crystallite size or coherence length (d) for Cu and Ni as a function of t for $Cu_{50}Ni_{50}$ and $Cu_{20}Ni_{80}$ blends. In either case, d for both Cu and Ni decreases with an increase in t and merges with each other after about 20 h. Finally, d reaches a minimum (d_{min}) of 31 and 18 nm for $Cu_{20}Ni_{80}$ and $Cu_{50}Ni_{50}$, respectively (Fig. 6). It has been pointed out by Eckert *et al.* [40–42] that d_{min} attainable under a given milling condition depends on the extent of recovery and solid solution hardening of the alloy in the course of MA. It is known that Cu–Ni system exhibits an f.c.c. structure over the entire composition range and addition of Cu to Ni produces a typical solid solution hardening in a polycrystalline alloy with grain size ≥ 1 μm [43]. Similar solid solution hardening may account for the smaller d_{min} in $Cu_{50}Ni_{50}$ as compared to that in $Cu_{20}Ni_{80}$. However, the present data are at variance with the recent observation of solid solution softening of Cu alloyed nanocrystalline Ni by Shen and Koch [44].

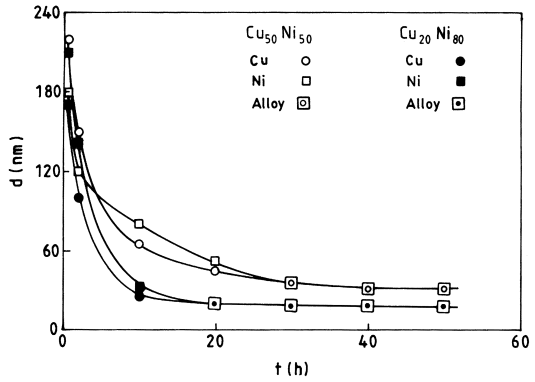

Fig. 6. Experimental data on variation of crystallite size (d) with milling time (t) of Cu and Ni in the $Cu_{20}Ni_{80}$ and $Cu_{50}Ni_{50}$ blends.

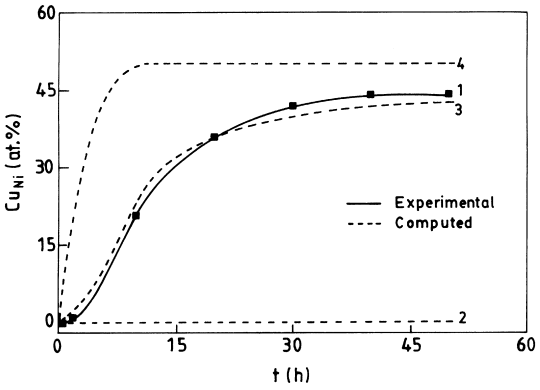

Fig. 7. Variation of Ni-content in Cu-solid solution (Cu_{Ni}) with milling time (t) for $Cu_{50}Ni_{50}$ blend milled at 300 rpm. Curve-1 represents the experimentally determined data. Curve-2, curve-3 and curve-4 are computed data obtained for $D = D_v$ (at $T = 553$ K), $D = D_v$ ($T_{eff} = 775$ K) and $D = D_{gb}$ ($T = 373$ K), respectively.

4.2. Solid solubility

It is known that the relative position of the XRD peaks from a single phase alloy is a function of the composition of the alloy. In the present study, the XRD peaks of Ni and Cu undergo a gradual shift towards each other as t increases. The extent of shift is more for Cu peaks than that in Ni, indicating faster enrichment of Ni in Cu than the reverse. Cu–Ni being an isomorphous system, this may be attributed to the faster diffusion coefficient of Ni in Cu, than that of Cu in Ni [45]. The gradual merger of the Cu and Ni peaks and continuous variation of d with t for both suggest that the diffusive intermixing mechanism is operative in the present system [27, 28]. It may be noted that the enthalpy of mixing (ΔH_m) for Cu–Ni alloys (in the solid state) is only about 2 J/mol [46, 47], which is favorable for gradual diffusive intermixing [27]. The degree of alloying of Ni into Cu (say, Cu_{Ni}) with the progress of milling, as determined from the XRD peak shift for the $Cu_{50}Ni_{50}$ blend, is shown by curve-1 in Fig. 7. A similar trend has also been recorded for the $Cu_{20}Ni_{80}$ composition (curve-1 in Fig. 8).

In order to compare the experimental data on the variation of Cu_{Ni} vs t with the predictions of the MICCM model, the experimental data on the variation of d for Cu and Ni (Fig. 6) has been used in the computation as the input data for d as a function of t. It implies that the lower limit of the layer thickness corresponds to the coherence length determined by XRD analysis, and hence, computation would predict the lower limit of the time required for intermixing. It may be mentioned that a possible change in the average diffusion field width caused by any extensive penetration of shear bends of different constituents can also be reflected in the measured value of d, that has been used as an

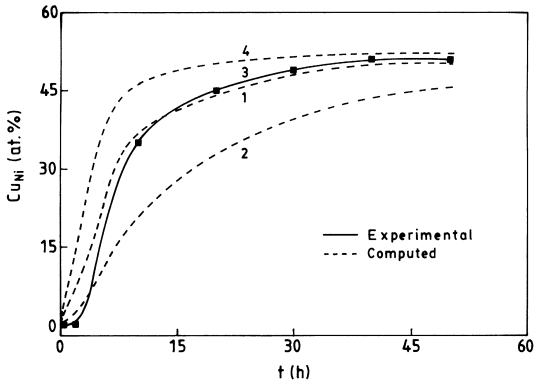

Fig. 8. Variation of Ni-content in Cu-solid solution (Cu_{Ni}) with milling time (t) for $Cu_{20}Ni_{80}$ milled at 300 rpm. Curve-1 represents the experimentally determined data. Curve-2, curve-3 and curve-4 are computed data obtained for $D = D_v$ (at $T = 745$ K), $D = D_v$ ($T_{eff} = 785$ K) and $D = D_v$ ($T = 825$ K), respectively.

input. A sharp composition gradient at the interface between the A and B regions depicted in Fig. 2 is, however, not expected in an isomorphous system like Cu–Ni. In order to apply the present MICCM formulation to the Cu–Ni system, it is assumed that the respective Ni contents at the interface between the Cu-rich and Ni-rich regions are 45 at.% and 55 at.%. D, necessary as an input data in the MICCM model, is fortunately available as a function of temperature (T) for different compositions of Cu–Ni alloys [48, 49]. At a given T, D vs C values have been fitted to a fourth order polynomial to determine D for a given concentration node in Fig. 3.

Computer analysis [8, 20, 50] has shown that the localized temperature at the point of impact between the ball and powder does not exceed 500 K. Furthermore, the experimental results of ball milling of steel powders with martensitic structure has evidenced that the local temperature rise should not exceed 538–553 K [16, 19]. If the alloying is assumed to take place by volume diffusion at $T = 553$ K (i.e. maximum attainable T during MA), the kinetics of MA predicted by the MICCM model (curve-2 in Fig. 7) in terms of the variation of Cu_{Ni} with t are more than two order of magnitude slower than the corresponding experimental data (i.e. curve-1 in Fig. 7). Therefore, volume diffusion does not seem to make any significant contribution to the process of MA, which incidentally substantiates a similar observation earlier reported by Wang *et al.* [51].

Earlier kinetic studies on cluster assembled nanocrystalline Cu have yielded exceptionally high self diffusivity values in these materials [2, 52, 53]. Therefore, it is of interest to find out whether the rate of mass transfer operative in MA reaches the level of concerned grain boundary chemical diffusivity (D_{gb}). Using the extrapolated D_{gb} values of Cu–Ni system at 373 K [45], the kinetics predicted by MICCM model (curve-4 in Fig. 7) is found to be more than an order of magnitude faster than the corresponding experimental data (curve-1 in Fig. 7). Thus, the actual atomic transport rate in MA seems to be faster than that for volume diffusion, but appreciably slower than the same for grain boundary diffusion at the milling temperature.

4.3. *Effective temperature for alloying*

In order to derive a better understanding of the kinetics of intermixing, volume diffusivity (D_v) values at different T have been used as the input along with the experimentally determined data on d as a function of t for $Cu_{50}Ni_{50}$ and $Cu_{20}Ni_{80}$ (Fig. 6) to simulate the variation of Cu_{Ni} with t in each composition in the course of MA. The temperature at which the theoretical predictions by MICCM model shows best agreement with the experimental data on the variation of Cu_{Ni} as a function of t, may be defined as the effective temperature of diffusive alloying (T_{eff}). Thus, T_{eff} reflects a measure of the enhanced interdiffusivity (D_{eff}) operative in the process of MA. For $Cu_{50}Ni_{50}$ composition, curve-3 calculated for $T_{eff} = 755$ K, matches well with the experimental data of curve-1 in Fig. 7. Similar calculation for $Cu_{20}Ni_{80}$ yields $T_{eff} = 785$ K (curve-3 in Fig. 8). It is interesting to note that a moderate deviation from T_{eff} (say, ± 40 K) yields a significant change in the alloying kinetics (curve-2 and curve-4 in Fig. 8). Therefore, T_{eff} must be selected with an accuracy of ± 10 K to minimize the deviation of the predicted result from the experimental data. Table 1 shows that T_{eff} is a function of the composition of mechanically alloyed powder. However, it is important to point out that the normalized temperature ratio (θ_{eff}), defined as the ratio of T_{eff} to the corresponding liquidus temperature (T_L), are quite close to each other for both the Cu–Ni blends [54] (Table 1).

The variation of Zn-content in Cu rich α-phase (Cu_{Zn}) with t during MA of elemental Cu and Zn powders under identical milling medium (as in the present study) has earlier been reported by Pabi *et al.* [34, 35]. In order to verify the proposed hypothesis on T_{eff} and θ_{eff}, the alloying kinetics for the Cu–Zn blends (earlier reported) have been compared with the predictions of the MICCM model to obtain the corresponding T_{eff} and θ_{eff} values. For simplification of the present analysis, it is assumed that the β-phase is present in the MA product since $t = 0$. The volume fraction of β at $t = 0$ can be

Table 1. Summary of computer analysis of experimental data through MICCM model

Composition	Ω rpm	T_L (K)	T_{eff} (K)	θ_{eff}
$Cu_{70}Zn_{30}$	200	1217	505	0.42
$Cu_{70}Zn_{30}$	300	1217	520	0.43
$Cu_{60}Zn_{40}$	300	1170	560	0.48
$Cu_{50}Ni_{50}$	300	1580	755	0.48
$Cu_{20}Ni_{80}$	300	1670	785	0.47

estimated from the nominal composition of the blend. Furthermore, it is assumed that the compositions of α and β at the α–β interface during MA may be obtained from concerned equilibrium diagram [55].

For the present computation, the data on the variation of d with t for α in the Cu–Zn system (reported in [34, 35]) has been utilized. The bulk diffusivity values in α and β phases are available in the literature [56]. Using these data, the variation of Cu_{Zn} with t at different T has been computed by the MICCM model, and subsequently, compared with the existing experimental data [34, 35] for $Cu_{70}Zn_{30}$ composition milled at $\Omega = 200$ and 300 rpm. Figure 9 shows the best possible fits obtained in a manner similar to that applied to the Cu–Ni system. Here the experimental data lag behind the simulated data in the early stage of MA by about 2 h. This divergence can be attributed to the fact that formation of a measurable amount of β-phase in reality needs about 2 h of milling [34, 35], while the present computation assumes that β forms instantaneously during MA. The corresponding T_{eff} and θ_{eff} values obtained for $Cu_{70}Zn_{30}$ composition are tabulated in Table 1. The T_{eff} increases marginally from 505 to 520 K as Ω increases from 200 to 300 rpm (Table 1). In contrast, the alloying kinetics at 200 rpm seems to be remarkably slower compared to that at 300 rpm (Fig. 9), apparently due to the slower rate of reduction of d with t at 200 rpm [34, 35]. MA of the $Cu_{60}Zn_{40}$ blend has resulted in a single phase microstructure comprising α when milled for about 12 h at 300 rpm [34, 35]. Table 1 shows that T_{eff} and θ_{eff} of $Cu_{70}Zn_{30}$ blend are lower than those for $Cu_{60}Zn_{40}$ composition, even though T_L of the former composition is higher than that for the latter [55].

Comparison between the T_{eff} values of the Cu–Ni and Cu–Zn alloys milled under identical conditions (cf. Table 1) reveals that T_{eff} is much higher in the former system. Thus it appears that T_{eff} may not have any direct correlation with the adiabatic rise in temperature at the point of ballpower impact during MA. Furthermore, it is most interesting to note that θ_{eff} of all the alloys lies between 0.4 and 0.5. In other words, it seems possible to scale the operating mass transfer rate with T_L of the concerned systems, which may be useful for predicting the alloying kinetics. It may be pointed out that the mobility term in a recent dynamical approach of modelling [31] may not exhibit such a correlation. In fact, Martin [57] earlier suggested that the ballistic effect during ion beam irradiation may increase the configurational entropy, which is equivalent to a rise in the temperature of the system to T' ($> T$ = ambient temperature). Furthermore, it was proposed that T' is related T through the following relationship:

$$T' = T\left(1 + \frac{D_{bal}}{D_{chim}}\right) \tag{17}$$

where, D_{bal} and D_{chim} are the ballistic and chemical interdiffusion coefficients, respectively. It may be pointed out that D_{chim} is exponentially related with temperature, while D_{bal} is considered to be temperature independent [57]. In an attempt to extend the applicability of equation (17) to MA, T' may be considered as equivalent to T_{eff} (obtained from Table 1) and $T = 323$ K, i.e. the approximate temperature inside the most common mills [8]. This gives $D_{bal}/D_{chim} = 0.4$–1 for the T_{eff} data presented in Table 1. If T in equation (17) corresponds to the temperature at the point of ballpowder impact, it would have higher values (~538–553 K [8, 16, 19]), which would further reduce the ratio of D_{bal} to D_{chim}. Therefore, it appears, that if D_{bal} is correlated with T_{eff} through equation (17) (assuming $T' = T_{eff}$), it would not account for the orders of magnitude enhancement in the diffusivity (D_{eff}) encountered in MA.

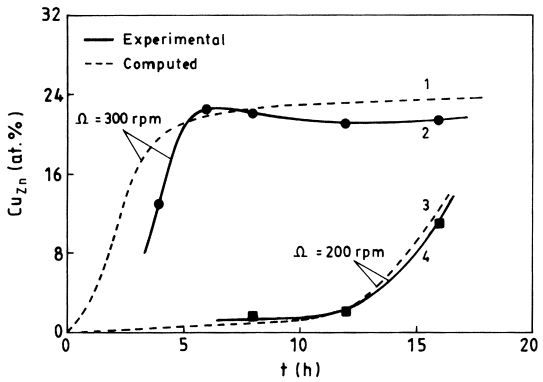

Fig. 9. Variation of Zn-content in Cu-solid solution (Cu_{Zn}) with milling time (t) for the $Cu_{70}Zn_{30}$ blend milled at 300 and 200 rpm. Curve-1 and curve-3 are computed for $D = D_v$ at $T = 520$ and 505 K, respectively.

In the MA process, microstructural refinement takes place as a result of sustained shear, repeated fracture and cold welding of particles [8, 11]. Hellstern *et al.* [4] have shown that the evolution of microstructure in MA takes place in several stages. All these factors make dynamic modelling of the MA process a formidable task. On the other hand, the present model yields a measure of the enhanced mass transfer rate in MA, which is supported by several experimental observations [23, 58–60]. This possibly indicates the dominant role of structural defects in the mass transfer process during plastic deformation concomitant with the process of MA. In this regard, earlier studies have reported that the diffusion coefficient of Ni is enhanced by several orders of magnitude in amorphous NiZr [58] and crystalline Ni–Al [59] during ball milling possibly due to a transient increase in free volume during plastic deformation. Hart [61] has shown that the bulk diffusion coefficient can be enhanced by dislocation short-circuiting, if a tracer atom visits many dislocations during the time of the experiment. Earlier, Balluffi and Ruoff [36] have concluded that

short-circuiting through moving grain boundaries and dislocations are responsible for the enhancement of diffusivity during plastic deformation. In general, the dislocations or grain boundaries sweeping through the crystals [62–64], excess vacancies created by deformation, or cooperative displacement of atoms by shear along randomly selected glide planes [31] may separately or in combination account for the enhanced mass transport rate during MA. The present study indicates that this enhanced diffusion rate may be correlated with the melting temperature of the system. However, further investigation is warranted to identify the precise contribution and mechanism responsible for this enhanced diffusion rate. Finally. it is apparent from the present study that the crystallite size of the constituents has to be reduced to nanoscale (< 100 nm) even in an isomorphous system like Cu–Ni for achieving a significant extent of alloying by high energy ball milling (Figs 6–8).

5. CONCLUSIONS

(1) A rigorous mathematical model of mechanical alloying (MA) in ductile miscible systems has been developed using a modified *iso*-concentration contour migration method. The model takes into account the variation of diffusion coefficient with composition, interface shift due to interdiffusion between adjacent phases, and change in of crystallite size of the constituent phases in the course of milling.

(2) The predictions of the model, when compared with the experimental data of MA for the Cu–Ni and Cu–Zn systems, indicate that volume diffusion has insignificant contribution to alloying. On the other hand, the rate of mass transport in MA seems to be slower than that for grain boundary diffusion. Thus, it appears that the effective mass transport operative in MA attains a rate intermediate between that for volume and grain boundary diffusion.

(3) An effective temperature for diffusive alloying (T_{eff}) has been proposed to simulate the observed alloying kinetics. T_{eff} does not appear to have any direct correlation with the localized temperature rise at the point of ball-power impact.

(4) T_{eff} is a function of the alloy composition. However, a change in milling speed from 200 to 300 rpm seems to have marginal effect on T_{eff} for the $Cu_{70}Zn_{30}$ blend.

(5) The normalized temperature ratio for all the Cu–Ni and Cu–Zn alloys studied is found to lie between 0.4 and 0.5. Thus, the effective mass transfer rate in MA seems to be related to the liquidus temperature of the systems studied.

Acknowledgements—The work is sponsored by the Department of Science and Technology, Government of India (Grant No.III.4(23)92-ET). The authors are thankful to C. Abromeit (HMI, Berlin) for a stimulating discussion.

REFERENCES

1. Gleiter, H., *Nanostruct. mater.*, 1992, **1**, 1.
2. Birringer, R., *Mater. Sci. Engng. A*, 1989, **117**, 33.
3. Suryanarayana, C., *Int. Mater. Rev.*, 1995, **40**, 41.
4. Hellstern, E., Fecht, H. J., Fu, Z. and Johnson, W. L., in *Multicomponent Ultrafine Microstructures*, ed. L. E. McCandlish, D. E. Polk, R. W. Siegel and B. H. Kear, Vol. 132. MRS Symp. Proc. Boston, MA, 1988, p. 137.
5. Hellstern, E., Fecht, H. J., Fu, Z. and Johnson, W. L., *J. Appl. Phys.*, 1989, **65**, 305.
6. Trudeau, M. L. and Schulz, R., *Mater. Sci. Engng A*, 1991, **134**, 1361.
7. Fecht, H. J., *Nanostruct. mater.*, 1992, **1**, 125.
8. Koch, C. C., *Processing of Metals and Alloys,* ed. R. W. Cahn, P. Haasen, E. J. Kramer, Vol. 15. VCH Publishers, Weinheim, 1991, p. 193.
9. Koch, C. C., *Nanostruct. mater.*, 1993, **2**, 109.
10. Pabi, S. K. and Das, A., *Met. Mater. Processes*, in press.
11. Benjamin, J. S., *Sci. Am.*, 1976, **234**, 40.
12. Murty, B. S., *Bull. Mater. Sci.*, 1993, **16**, 1.
13. Murty, B. S., Mohan Rao, M. and Ranganathan, S., *Acta metall. mater.*, 1995, **43**, 2443.
14. Bickerdike, R. L., Clark, D., Easterbrook, J. N., Hughes, G., Mair, W. N., Partridge, P. G. and Ranson, H. C., *Inter. J. Rapid Solidification*, 1984–85, **1**, 305.
15. Cardellini, F., Mazzone, G., Montone, A. and Antisari, M. V., *Acta. metall. mater.*, 1994, **42**, 2445.
16. Davis, R. M. and Koch, C. C., *Scripta metall.*, 1987, **21**, 305.
17. Green, M. L., Coleman, E., Bader, F. E. and Sproles, S. E., *Mater. Sci. Engng*, 1984, **662**, 231.
18. Yavari, A. R., *Mater. Sci. Engng A*, 1994, **179**, 20.
19. Davis, R. M., McDermott, B. T. and Koch, C. C., *Metall. Trans. A*, 1988, **19**, 2867.
20. Schwarz, R. B. and Koch, C. C., *Appl. Phys. Lett.*, 1986, **49**, 146.
21. Martin, G. and Gaffet, E., *J. Phys. France (Colloque)*, 1990, **51**, C4–71.
22. Aikin, B. J. M. and Courtney, T. H., *Metall. Trans. A*, 1993, **24**, 2465.
23. Schultz, R., Trudeau, M. and Huot, J. Y., *Phys. Rev. Lett.*, 1989, **32**, 2849.
24. Dupeux, M., Wan, C. and Willemin, P., *Acta metall. mater.*, 1993, **41**, 3071.
25. Courtney, T. H., Malzahn Kampe, J. C., Lee, J. K. and Maurice, D. R., *Diffusion Analysis and Applications*, ed. A. D. Romig and M. A. Dayananda. TMS Mineral and Material Soc., Warrendale, PA, 1989, p. 225.
26. Bhattacharya, A. K. and Arzt, E., *Scripta metall. mater.*, 1993, **28**, 395.
27. Pabi, S. K. and Murty, B. S., *Mater. Sci. Engng A*, 1996, **214**, 146.
28. Pabi, S. K., Joardar, J., Manna, I. and Murty, B. S., *Nanostruct. Mater.*, 1997, **9**, 149.
29. Chen, Y., Bibole, M., Le Hazif, R. and Martin, G., *Phys. Rev. B*, 1993, **48**, 14.
30. Martin, G. and Bellon, P., *Statics and Dynamics of Alloy Phase Formations*, ed. P. E. A. Turchi and A. Goris. NATO ASI Series, Vol. 319. Plenum Press, New York, 1994, p. 605.
31. Bellon, P. and Averback, R. S., *Phys. Rev. Lett.*, 1995, **74**, 1819.
32. Pabi, S. K., *Phys. status solidi (a)*, 1979, **51**, 281.
33. Murty, B. S., Singh, K. H. S. and Pabi, S. K., *Bull. Mater. Sci.*, 1996, **19**, 565.
34. Pabi, S. K. and Murty, B. S., *Bull. Mater. Sci.*, 1996, **19**, 939.

35. Pabi, S. K., Joardar, J. and Murty, B. S., *J. Mater. Sci.*, 1996, **31**, 3207.
36. Balluffi, R. W. and Rouff, A. L., *Appl. Phys. Lett.*, 1962, **1**, 59.
37. Guinier, A., *X-Ray Diffraction.* W. H. Freeman Publ., San Fransisco, 1963, p. 125.
38. Wilson, A. J. C., *Proc. Phys. Soc. (London)*, 1962, **80**, 286.
39. Coles, B. R., *A hand book of Lattice Spacings and Structures of Metals and Alloys,* ed. W. B. Pearson. Pergamon Press, London, 1958, p. 592.
40. Eckert, J., Holzer, J. C., Krill, C. E. and Johnson, W. L., *J. Mater. Res.*, 1992, **7**, 1751.
41. Echert, J., Holzer, J. C. and Johnson, W. L., *Scripta metall. mater.*, 1992, **27**, 1105.
42. Eckert, J., Holzer, J. C., Krill, C. E. III and Johnson, W. L., *J. Mater. Res.*, 1992, **7**, 1980.
43. Hu, G. X. and Qian, M. G., *Physical Metallurgy.* Shanghai Science and Technology Publisher, Shanghai, 1983, p. 298.
44. Shen, T. D. and Koch, C. C., *Acta metall. mater.*, 1996, **42**, 753.
45. Kaur, I., Gust, W. and Kozma, L., *Handbook of Grain and interface Boundary Diffusion Data,* Vol. 1. Ziegler Press, Stuttgart, 1989, p. 409.
46. Oriarni, R. A. and Murphy, W. K., *Acta metall. mater.*, 1960, **8**, 23.
47. Kubachewski, O., Dench, W. A. and Genta, V., *Physical Chemistry of Metallic Solutions and Intermetallic Compounds* (Proc. NPL Symp. No. 9). HMSO, London, 1958, p. 2.
48. Balakir, E.A., Zotov, Y.P., Malysheva, E.B., Panchishnyi, V.I., Padgorskii, B.N. and Sharapov, V.V., *Diff. Defect Data*, 1976, **12**, 49.
49. Maier, K., Bassani, C. and Schule, W., *Phys. Lett. A*, 1973, **44**, 539.
50. Bhattacharya, A. K. and Arzt, E., *Scripta metall. mater.*, 1992, **27**, 749.
51. Wang, Y. K., He, Q. A. and Wang, T. J., *Metall. Trans. A*, 1993, **24**, 225.
52. Birringer, R., Hahn, H., Fofler, H., Karch, J. and Gleiter, H., *Diff. Defect Forum*, 1989, **67**, 549.
53. Howath, J., Birringer, R. and Gleiter, H., *Solid State Commun.*, 1987, **62**, 319.
54. Chakrabarti, D. J., Laughlin, D. E., Chen, S. W. and Chang, Y. A., *Binary Alloy Phase Diagrams*, ed. T. B. Massalski, 2nd edn, Vol. 2. ASM Int. Mater. Park, OH, 1990, p. 1442.
55. Midowrik, A. P., *Binary Alloy Phase Diagram,* ed. T. B. Massalski, Vol. 2. ASM Metals Park, OH, 1986, p. 1508.
56. Smithells, C. J. and Brandes, E. A. (ed.), *Metals Reference Book,* 5th edn. Butterworths, London, 1976, p. 895.
57. Martin, G., *Phys. Rev. B*, 1984, **30**, 1424.
58. Mazzone, G., Montone, A. and Vittori Antisari, M., *Scripta metall. mater.*, 1993, **28**, 821.
59. Cardellini, F., Mazzone, G., Montone, A. and Vittori Antisari, M., *Acta metall. mater.*, 1994, **42**, 2445.
60. Kaper, N., Kyllesbech Larsen, K. and Bottiger, J., *Philos. Mag. B*, 1992, **66**, 507.
61. Hart, E. W., *Acta metall.*, 1957, **5**, 597.
62. Tracy, J. M. and Groza, R. J., *Nanostruct. mater.*, 1992, **1**, 369.
63. Belyakava, N. M., Zholud, V. V., Larikovand, N. L. and Mozanko, F. V., *Matallofizika*, 1992, **14**, 96.
64. Bhattacharya, A. K. and Arzt, E., *Scripta metall. mater.*, 1992, **27**, 635.